LA-UR-21-23241
Accepted Manuscript

Validation of neutron-induced reactions on natural carbon using an active target at neutron energies up to 22 MeV at LANSCE

Kuvin, Sean Andrew
Lee, Hye Young
DiGiovine, Brad Joseph
Georgiadou, Anastasia
Mosby, Shea Morgan
Votaw, Daniel Gregory Jenks
White, Morgan Curtis
Zavorka, Lukas

Provided by the author(s) and the Los Alamos National Laboratory (2022-02-25).

To be published in: Physical Review C

DOI to publisher's version: 10.1103/PhysRevC.104.014603

Permalink to record:
http://permalink.lanl.gov/object/view?what=info:lanl-repo/lareport/LA-UR-21-23241

Los Alamos National Laboratory, an affirmative action/equal opportunity employer, is operated by Triad National Security, LLC for the National Nuclear Security Administration of U.S. Department of Energy under contract 89233218CNA000001. By approving this article, the publisher recognizes that the U.S. Government retains nonexclusive, royalty-free license to publish or reproduce the published form of this contribution, or to allow others to do so, for U.S. Government purposes. Los Alamos National Laboratory requests that the publisher identify this article as work performed under the auspices of the U.S. Department of Energy. Los Alamos National Laboratory strongly supports academic freedom and a researcher's right to publish; as an institution, however, the Laboratory does not endorse the viewpoint of a publication or guarantee its technical correctness.

Validation of neutron induced reactions on natural carbon using an active target at neutron energies up to 22 MeV at LANSCE

S. A. Kuvin,* H. Y. Lee, B. DiGiovine, A. Georgiadou, S. Mosby, D. Votaw, M. White, and L. Zavorka†
Los Alamos National Laboratory, Los Alamos, NM 87545, USA
(Dated: February 24, 2022)

A single crystal Chemical Vapor Deposited (sCVD) diamond detector is used as an active target to measure neutron induced reactions on natural carbon using the neutrons produced by spallation, with a broad energy spectrum at LANSCE. The neutron-induced reactions are detected in the diamond as low as E_n = 400 keV and up to approximately 100 MeV. Relative cross sections for ^{12}C(n,α_0), ^{12}C(n,p$_0$), ^{12}C(n,d$_0$+p$_1$), and ^{13}C(n,α_0) are reported up to E_n = 22 MeV and comparisons on detected pulse height spectra and detector response of scattering reactions are made with GEANT4 simulations using the ENDF/B-VIII.0 evaluated nuclear data library up to 20 MeV. The results are compared with past experimental data, including other works that incorporate diamond detectors as an active carbon target. In addition, R-matrix calculations for the ^{13}C + n system are presented.

I. INTRODUCTION

Neutron-induced charged-particle (n,z) reactions are ubiquitous in nature and, as a result, there is a need for precise nuclear reaction data for a variety of applications. At the Weapons Neutron Research (WNR) facility at the Los Alamos Neutron Science Center (LANSCE) [1], the Low-Energy Neutron induced charged-particle (Z) (LENZ) collaboration has been studying these reactions to address nuclear data needs for characterizing gas production in structural materials [2, 3], provide precision measurements of key reactions like ^{16}O(n,α) [4] and ^{35}Cl(n,p) [5], and reaction studies involving radioactive targets [6] for both applied and astrophysical interests [7].

Among the many key reactions for which precise nuclear data are required, reactions on elemental carbon are particularly prolific for obvious reasons. Neutron elastic scattering and total cross section measurements on elemental carbon have been well studied and the evaluations of elastic scattering data are considered a standard up to approximately 1.8 MeV. However, extending neutron induced reaction evaluations on carbon as a reference standard at higher energies, including inelastic channels and (n,z) reactions, is necessary to benefit multiple applications that are sensitive to reactions with carbon at energies higher than 2 MeV. One such reason is due to the growing prevalence of applying diamond detectors as neutron spectrometers [8–15], for which the ^{12}C(n,α) reaction is particularly important. Specifically, the use of diamond detectors as a neutron flux monitor for D-T neutron generators would require high-precision characterization up to and around 14 MeV.

For the ^{13}C(n,α)^{10}Be reaction, cross section measurements can be used to study the time-reverse ^{10}Be(α,n)^{13}C reaction cross section using the detailed balance theorem. Because ^{10}Be is a radioactive nucleus ($T_{1/2}$ = 1.51×10^6 years), no direct (α,n) cross section measurements have been reported. Therefore, for astrophysical applications such as Big-Bang Nucleosynthesis, nuclear network calculations still use the reaction rate that was predicted theoretically in 1969 [16] and is highly uncertain. Therefore, by providing new cross section measurements on ^{13}C(n,α)^{10}Be, the rate for the inverse reaction can be better constrained.

TABLE I. Run summary for the data taken with the diamond detector at flight path 90L at WNR.

Average LANSCE proton current	2 μA
Data collection time	1 hour
Diamond detector thickness	0.5 mm
Detector bias	+502V
Timing resolution	1.0(1) ns
Distance from neutron source	7618(2) mm
E_n resolution (E_n = 0.4 MeV)	2 keV
E_n resolution (E_n = 2 MeV)	13 keV
E_n resolution (E_n = 20 MeV)	350 keV

At LANSCE, diamond detectors are being explored as an alternative to silicon for spectroscopy studies of (n,z) reactions with radioactive targets. As part of this effort, a Cividec B8 sCVD diamond detector [17] was studied by placing it along the beam axis to detect the fast neutrons, with a broad energy spectrum, that are produced by the unmoderated spallation neutron source. The original goal of this study was to characterize the expected backgrounds for using diamond detectors for charged particle spectroscopy. However, by using the diamond detector as an active carbon target and extracting the incident neutron energy from time of flight, neutron-induced cross sections on natural carbon could be measured over a wide range of energies for both scattering and charged particle reactions, all at once. The results presented in this work are used to validate simulations that incorporate available evaluations as inputs and to inform the current status of nuclear data evaluations on carbon.

* kuvin@lanl.gov
† Current affiliation: Oak Ridge National Laboratory

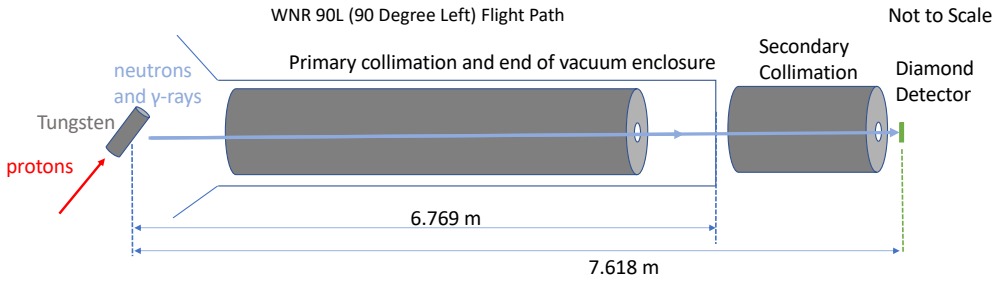

FIG. 1. A sketch of the 90 degree flight path at the WNR Facility. The 4 × 4 mm^2 Cividec B8 diamond detector is placed downstream of the secondary collimation.

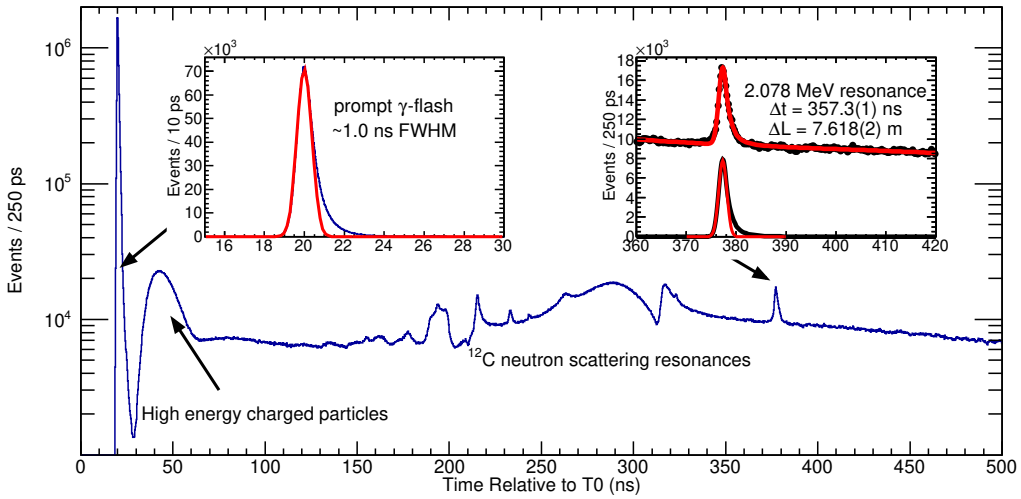

FIG. 2. Timing spectrum relative to the proton pick-off reference, as recorded by the diamond detector. The insets show the peaks originating from the prompt γ-flash and from the 2.078 MeV scattering resonances. The time difference between these peaks is used to calibrate the flight path length between the diamond and the WNR spallation neutron source.

II. EXPERIMENT

The LANSCE accelerator delivered 800 MeV protons to the un-moderated Tungsten target at WNR, producing fast neutrons via spallation. The diamond detector was placed upstream of the LENZ experimental chamber [18], along the beam axis, and its location was measured relative to the chamber and the upstream collimation. A sketch of the experimental setup at the 90 degree (90L) flight path at the WNR facility is shown in Fig. 1. Specific details about the design of the diamond detector are well documented in Refs. [17, 19, 20]. The beam was collimated down to a 6 mm diameter that is slightly larger than the active area of the diamond detector (4 mm x 4 mm) and only the tails of the beam will overlap with the aluminum plate used to support the detector housing. The dominant sources of downscatter are expected to come from the nearby collimation, detector housing and PCB material.

For the current experiment, we employed the C6 charge-sensitive preamplifier provided by Cividec and the 500 μm thick detector was biased to +502V. The single output channel from the diamond detector was fed into the existing digital data acquisition(DAQ) stream from the LENZ experiment that was already in progress. The DAQ consists of 16-channel CAEN VX1730 digitizers that are programmed with CAEN DPP-PSD firmware with all channels triggering independently and determined by a leading edge discriminator. The rise time and FWHM of the diamond detector signals were approximately 8 ns and 20 ns, respectively. For each triggered event a waveform consisting of 64 samples (128 ns) was recorded, including 60 ns of trace recorded before the trigger timestamp. This particular setup is similar to that of Ref. [21], where they also characterized the effect on energy resolution for the 500MS/s CAEN DT5730

digitizers in comparison to a faster sampling 1GS/s digitizer but with less ADC resolution (10-bit as opposed to 14-bit). Their comparison showed a slight reduction in energy resolution that was tolerable in exchange for the higher data throughput of the 500MS/s digitizer.

The time structure of the LANSCE proton beam consisted of 40 macropulses/second, with each 625 μs long macropulse consisting of approximately 340 micropulses, each separated by 1.8 μs. The average trigger rate for the detector was around 8 kHz and no sign of degradation or polarization was observed in the 1 hour period that the detector was in the beam axis. The average data rate was low relative to the data throughput limits and due to the fast timing of the detector and the fast sampling rate, dead-time corrections were negligible.

During this period, the LENZ annular silicon detectors and the flux monitor ionization chamber [22] continued to take data. An uptick in silicon detector events were observed due to increased scatter off the diamond detector and housing. Ionization chambers [22] loaded with ^{238}U and ^{235}U foils were used to characterize the shape of the neutron flux above and below 2 MeV, respectively.

The relative time between the proton pickoff signal ("T0") just before the WNR spallation target and the diamond detector is shown in Fig. 2. The dominant peak is due to the prompt γ-flash that comes from the spallation target. Here, the measured timing resolution is around 1 ns FWHM which is reasonable considering the sampling limitations on such a fast signal. Intrinsic diamond detector timing resolutions have been reported as low as tens of picoseconds [23].

Delayed events are measured relative to this prompt signal to determine the incident neutron energy. Structures are observed among these delayed events that are consistent with ^{12}C+n scattering resonances. From here, the diamond detector data was used to inform LENZ measurements by providing an additional (and precise) determination of the flight path length [5]. This was accomplished by measuring the time difference between the mean value of the γ-flash and the mean value of the 2.078 MeV neutron scattering resonance. An uncertainty of 0.1 ns for the time difference was obtained by varying the line-shapes that are used to fit the peaks to better reproduce the observed delayed tail. With the known energy of the 2.078 MeV resonance and a measured time of flight (with respect to the γ-rays) of 357.3(1) ns we get a flight path length of 7.618(2) m. This value was more precise than the capabilities of the flight path surveying methods used at the time, but recent upgrades to WNR target fiducials allow for the location of the spallation target to be measured with respect to the experimental areas at the sub-mm level. In addition, enough data for this resonance could be recorded in a matter of minutes so the diamond detector is a very useful tool for making quick flight path length measurements at WNR.

The different reaction channels that contribute to the time of flight spectrum can be seen in the plot of detected charged particle energy versus time as shown in Fig. 3. Here we identify reactions due to neutron elastic scattering and multiple scattering on carbon, as well as ^{12,13}C(n,α)^{9,10}Be and ^{12,13}C(n,p)^{12,13}B reactions. High-energy incident charged particles that come with the beam are observed but are a small component below 20 MeV in incident neutron energy. These particles, when present at high incident energies, punch through the detector before depositing their full energy and at higher incident energies result in an increased low-energy background. As shown in Ref. [24], these minimally ionizing particles can potentially be identified and vetoed through pulse shape analysis when appropriate electronics are employed. At WNR, the use of an additional dipole sweeping magnet after the secondary collimation can also reduce this source of background. Finally, at lower incident neutron energies, the highest detected energy events are identified as being due to ^{14}N(n,p)^{14}C (Q-value = +0.62 MeV). As discussed in Section IV, these events appear to be predominately due to (n,p) reactions on the nitrogen content in air that occur close to the diamond detector rather than due to the nitrogen content within the electronic-grade diamonds (< 5 ppb nitrogen and boron).

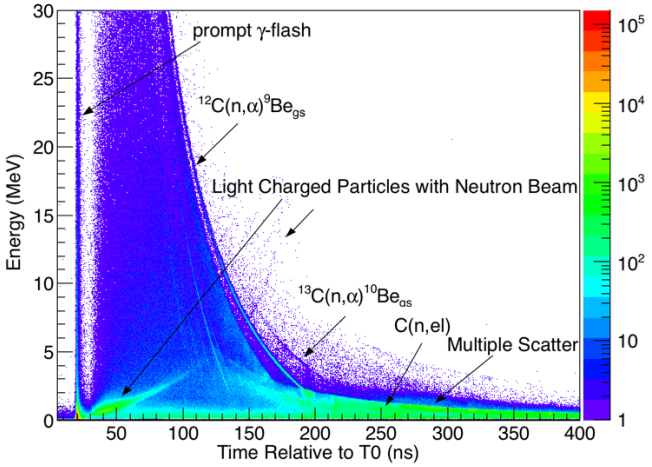

FIG. 3. The detected pulse height spectra as a function of relative time-of-flight (related to the incident neutron energy). Different reaction channels are identified based on the energy deposited for a particular incident neutron energy.

Once the flight path length was determined, the pulse height spectrum was internally calibrated based on the detected reaction channels, including ^{12}C(n,α) at neutron energies above 8 MeV and the blurred upper edge of the elastic scattering spectra (corresponding to neutrons scattered at 180 degrees) at lower energies. Consistent with Refs. [20] and [25], the measured pulse height values showed good linearity with the expected energies. At the higher incident neutron energies, the total energy resolution is dominated by the 1 ns timing resolution, as shown in Table I. The detected-energy resolution was

then determined by comparison with the GEANT4 simulation [26], discussed in the next section, by first folding in the timing resolution of the detector and then extracting an approximately 85 keV energy resolution (FWHM), needed for better agreement between data and the simulated pulse height spectra at lower incident neutron energies (*i.e.* corresponding to detected ^{12}C ions and α-particles at energies below 3 MeV). The detected-energy resolution improves with increasing amplitude; however, the total resolution is typically compensated by the worsening neutron energy resolution (from time-of-flight) as the incident neutron energy increases. In comparison, a 100 keV (1.75%) resolution was measured at 5.5 MeV with an external alpha source, and a similar amplifier, in Ref. [21]. As stated in the same reference, improved energy resolutions can be obtained with a better-suited spectroscopic amplifier, at the expense of the fast-timing (high-rate) properties of the current amplifier, or with a digitizer setup better matched for the fast signals.

For more discussion on the properties and the performance of the diamond detectors and electronics, including the pulse-height linearity, charge collection efficiency, sources of pulse height deficits, and intrinsic energy and timing resolutions, we point to Refs. [21], [25], the thesis work of Weiss [20], and the references therein. The work of Ref. [20] also details the use of diamond detectors for charged particle spectroscopy at a neutron time of flight facility and their study of ^{59}Ni(n,α) [19] served as a proof of principle for such measurements. The current results from our study indicate the feasibility of having a compact setup of diamond detectors placed close to the target/beam axis, to optimize geometric efficiency without significant loss of performance, for measurements at the WNR facility at LANSCE. The application of diamond detectors at WNR studying (n,p) and (n,α) reactions with a ^{58}Ni target will be discussed as part of a future instrumentation paper. That work featured the same diamond detector used in this work, but with a spectroscopic amplifier better suited for in-vacuum operation of the detector where longer cables (resulting in a higher input capacitance) are required.

Finally, after applying a linear energy calibration, the detection threshold was determined to be $\approx$ 180 keV. At a flight path length of 7.618 m from the spallation neutron source, coupled with the 1.8 μs pulse spacing, the lowest neutron energies that can be observed before frame overlap occurs is $\approx$ 100 keV. Therefore, no wraparound events are expected from the detection of lower energy neutrons. As a result, this flight path length at WNR is ideal for measuring neutron energies down to the detection threshold. On the other hand, better energy resolution at higher incident neutron energies can be achieved by going to longer flight paths at WNR such as the 15 degree flight path (L > 13 m) at the expense of frame overlap beginning to occur at 300 keV (unless the time between pulses is increased from 1.8 μs).

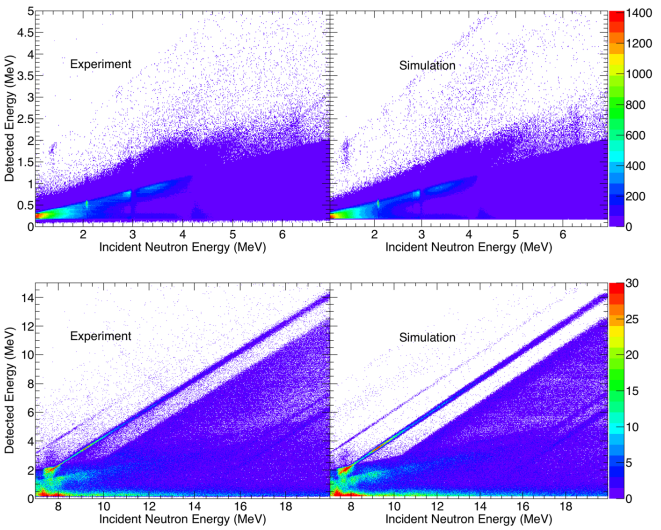

FIG. 4. Detected pulse height spectra, with a comparison to a GEANT4 simulation using the ENDF/B-VIII data library, as a function of incident neutron energy for the (top panels) low energy regime that is dominated by elastic scattering and (bottom panels) the energy regime above 7 MeV where (n,z) reaction channels are open.

III. SIMULATION

A GEANT4 [26] study, simulating the detection of γ-rays and neutrons by the diamond detector was developed to compare with the measured detector response. The simulation takes the shape of the broad neutron energy spectrum as an input and impinges the neutrons on the front face of the diamond detector. For simplicity, only the material that is in close proximity to the active diamond volume is considered (e.g. the detector housing and mounting frame). The detector housing consists of PCB material with thin gold plating around the entire area.

The simulations in this work were performed with GEANT version 4.10.02 and utilized the most recent ENDF/B-VIII.0 library [27]. As discussed in Ref. [28], the multi-step process that leads to the breakup of ^{12}C into three α particles is not treated properly by GEANT4 with standard options, aside from the direct ^{12}C(n,nα)^{8}Be $\rightarrow$ α+α channel. For example, inelastic scattering to ^{12}C states above the α- separation energy will de-excite by γ- emission even if they have a 100% α- branching ratio. Detector response simulation codes for organic scintillators like NRESP [29] properly treat these reactions and Ref. [28] incorporated the NRESP treatment of the breakup into GEANT4. Similarly, the NRESP code was modified from its original use to simulate the response of diamond detectors [30]. To make use of the modifications of Ref. [28] in recent versions of GEANT4, one should set the environment variable G4PHP_USE_NRESP71_MODEL to 1 [28, 31].

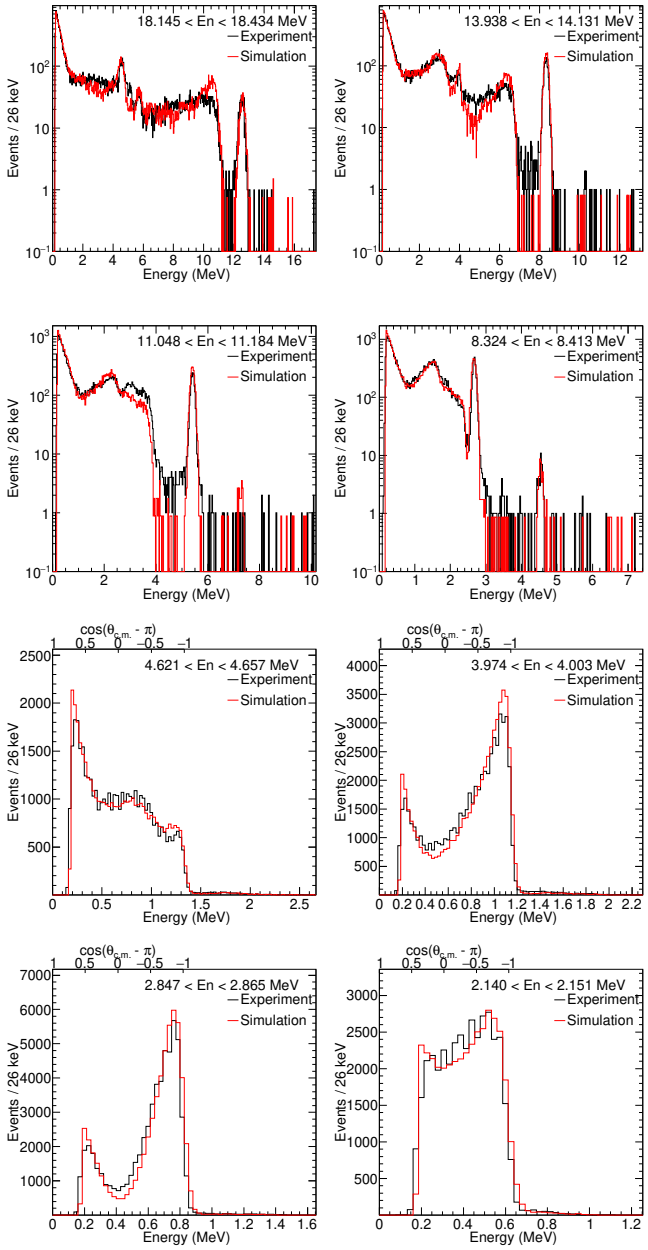

FIG. 5. Pulse height spectra for a few selected energy bins for the top four panels. For the bottom four panels, the spectra are dominated by neutron elastic scattering and the corresponding c.m. angle, that is proportional to the recoiling ^{12}C energy, is shown along the top axis. The data shows good qualitative agreement with the simulation.

In this work, for simplicity, we make a first order correction by post processing the events that lead to α- unbound states in ^{12}C, to perform a sequential decay of $^{12}\mathrm{C} \rightarrow \alpha + {}^{8}\mathrm{Be} \rightarrow \alpha + \alpha$ and to treat all of the outgoing charged particle energy as being detected regardless of interaction depth in the diamond with the assumption of isotropic distributions in the c.m. frame. After doing

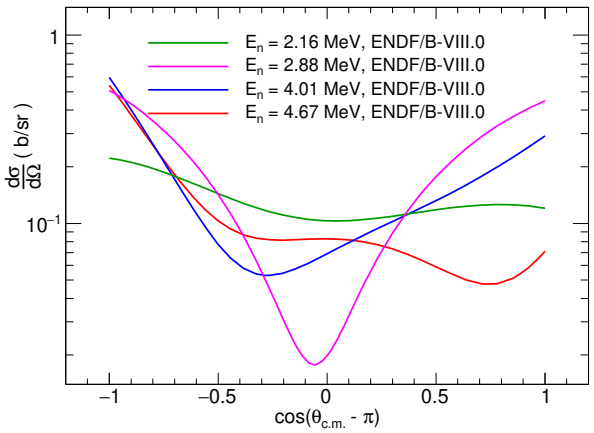

FIG. 6. Angular distributions from ENDF/B-VIII.0 are shown for comparison with the low energy panels of Figure 5 to elucidate how the distribution of scattering angle leaves an imprint on the detected ^{12}C recoil energies.

this, the comparison between simulation (right panels) and experiment (left panels) is qualitatively very similar as shown in Figure 4.

The $\beta-$ decay of unstable isotopes that are produced in the reactions and come to a rest within the diamond detector, such as ^{12}B ($T_{1/2}$ = 20.2 ms), ^{13}B ($T_{1/2}$ = 17.33 ms), and to a lesser extent ^{10}Be ($T_{1/2}$ = 1.51 x 10^6 year), lead to a quasi-uncorrelated low energy background although these events represent a small fraction when compared to the correlated neutron induced events above 1 MeV.

IV. COMPARISONS WITH SIMULATION

A. Neutron elastic scattering on ^{12}C

At incident neutron energies below 4.5 MeV, the observed spectrum is dominated by neutron elastic scattering on ^{12}C. However, a small number of counts due to ^{14}N(n,p) are also observed in this energy range. In the simulation these events are tracked and mostly originate from (n,p) reactions on air, close to the detector, instead of from within the diamond detector itself. The top four panels in Figure 5 compare the measured pulse height spectra with the simulations for selected neutron energies.

In this energy range, the elastically scattered ^{12}C ions are detected with a continuous distribution of energies that reflect the missing energy from the un-detected scattered neutron. Because the energy of the scattered neutron (and ^{12}C ion) is sensitive to the scattering angle, the angular distribution of the outgoing neutron leaves an imprint of the missing energy on the detected energy, as shown in the lower four panels of Fig. 5 for a few se-

lected incident neutron energy ranges. For these spectra, the x-axis label at the bottom shows the detected energy and the x-axis label at the top shows the corresponding non-relativistic c.m-angle, of the scattered neutron, as given by:

$$\cos(\theta_{cm}) = 1 - \left(\frac{E_{det}}{E_n} \frac{(M_n + M_{^{12}C})^2}{(2M_n M_{^{12}C})} \right) \qquad (1)$$

where E_{det} is the detected ^{12}C recoil energy in the laboratory frame, E_n is the reconstructed incident neutron energy in the laboratory frame. As previously mentioned, the threshold in the simulation has been adjusted to reproduce the experimental thresholds and the simulated spectra in each panel of Fig. 5 has been independently normalized to match the integral of the experimental yield above $\cos(\theta_{cm} - \pi) > 0$. The events that lie above the blurred edge at $\cos(\theta_{cm} - \pi) = 1$ are due to multiple scatter events where the scattered neutron has a second chance at depositing additional energy. The simulation does reasonably well in reproducing these multiple scatter events.

Clearly, for neutron detection at this energy range, the efficiency of the detector is most sensitive to the angular distributions of the scattered neutrons and the energy detection threshold of the detector. Conversely, the experimental data provides a very sensitive test of the angular distributions from evaluated data libraries that are used as inputs in the simulations. The corresponding angular distributions from ENDF/B-VIII.0, at consistent energy for the spectra in the bottom four panels of Fig. 5, are shown in Fig. 6 and illustrate the energy dependence of the angular distribution. Our experimental data indicates that the shape of the angular distributions for nearly all of the energy bins, where neutron elastic scattering dominates, is qualitatively consistent. This highlights the quality of both the measured and evaluated data for this reaction channel.

From this we conclude that the pulse height spectra can be used to validate evaluated scattering differential cross section data through comparison with simulations and by using a forward propagation method. However, a more direct comparison with past experimental data should be possible, due to the direct correlation between outgoing recoil energy and scattering angle. This approach would require more characterization of the detector response matrix, which is beyond the scope of this current paper.

B. Inelastic Scattering

At incident energies above 4.74 MeV, the first inelastic scattering channel opens up leading to the first excited state in ^{12}C at E_x = 4.44 MeV. Since this state is bound with respect to α- emission, the use of γ-ray tagging along with a diamond detector to isolate the

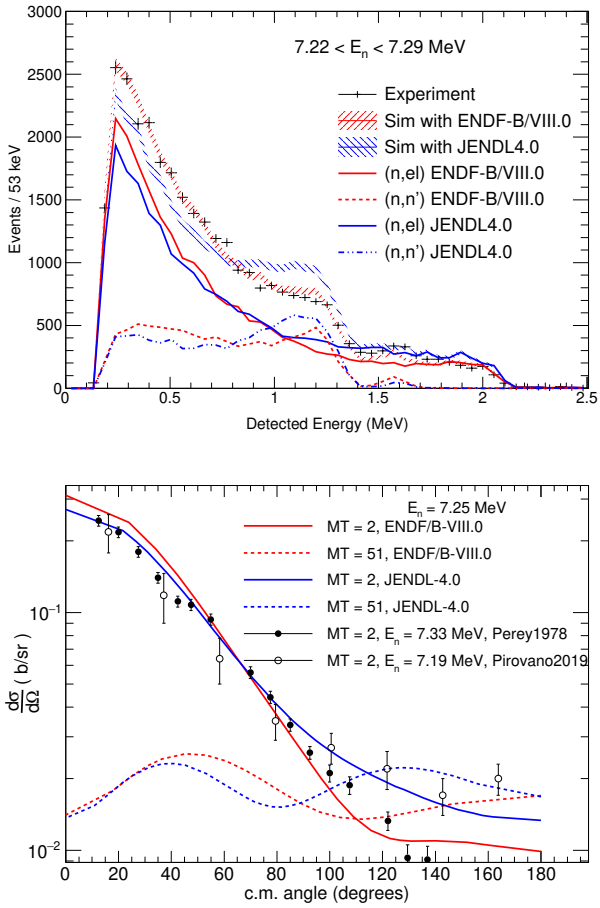

FIG. 7. The top panel shows the measured pulse height spectra at an incident neutron energy, for which the spectra is dominated by both elastic scattering (MT = 2) and inelastic scattering to the first excited state in ^{12}C (MT = 51). Although the reaction channels cannot be completely disentangled, the imprint of the evaluated angular distributions (bottom panel) is shown on the simulated spectra for two different evaluations [27, 32]. The experimental data, for this energy bin, is more consistent with the forward peaked evaluation of ENDF/B-VIII.0 [27]. Previous experimental data [33, 34] from nearby energies are also shown in the bottom panel for comparison

contributions from this reaction channel could be performed at WNR to compare experimental results with simulations as in the previous section. However, even without disentangling the elastic channel from the inelastic channel, a qualitative analysis of the pulse height spectrum can be used to validate the simulations that incorporate different evaluations, as shown in the top panel of Fig. 7 for the energy range between 7.22 and 7.29 MeV. The corresponding angular distributions from JENDL-4.0 [32] and ENDF/B-VIII.0 [27] for this energy range, along with experimental data at nearby energies [33, 34], are shown in the bottom panel of Fig. 7. Here,

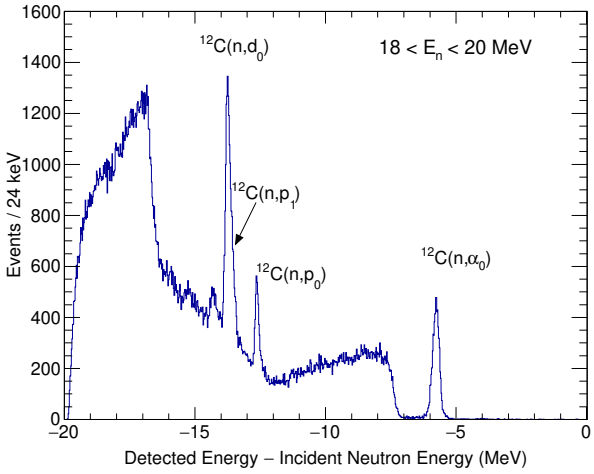

FIG. 8. A projection of Fig. 4, for incident neutron energies between 18 and 20 MeV, after subtracting the incident neutron energy from the detected energy to obtain the Q value for the reaction channel.

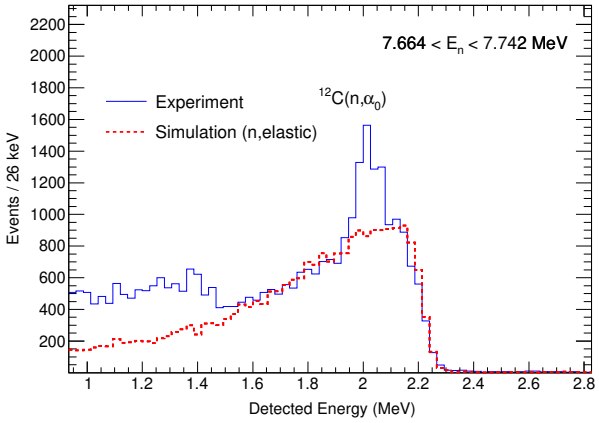

FIG. 9. At energies above 8.2 MeV, the (n,α) peak can be discriminated from other reaction channels as shown in Fig. 8. However, at lower energies, the elastic scattering events form a background underneath the (n,α) peak. To obtain the (n,α_0) yield at these energies, we assume that the elastic scattering data is well constrained and perform a background subtraction using the simulated (n,el) spectra by scaling the shape to match nearby detected energy bins.

we see that the angular distributions from JENDL-4.0, for both the elastic and inelastic channels, are less forward focused than with ENDF/B-VIII.0. As a result, the simulation that incorporates the JENDL-4.0 library appears to be inconsistent with the measured pulse height spectrum that shows an energy distribution that is more consistent with ENDF/B-VIII.0 library. As a disclaimer, this energy range was chosen to simply highlight how the pulse height spectra can be used to guide future evaluations through a forward propagation method and does not speak to the validity of one evaluation over another for all of the neutron energy bins.

Higher excited states in ^{12}C are all unbound with respect to α- emission, however, as mentioned in Section III, the default behavior in GEANT4 appears to de-excite these states by γ- emission rather than reflecting the fact that these states lie above the threshold for triple α breakup. In the current simulation, these events are recovered through post-processing but the NRESP treatment previously discussed can also be employed in more recent versions of GEANT4. Once again, future efforts may also include adding additional auxiliary detectors to detect scattered neutrons and further constrain the kinematics for the reactions occurring within the diamond detector.

Comparison between simulation and experiment at a few selected incident neutron energies above 8 MeV are shown in the top four panels of Fig. 5. Here, the simulated spectrum is normalized to the experimental data independently for each energy bin and the results show reasonable agreement in the shape of the spectrum, although there is clearly a potential need for better characterization of the individual inelastic scattering channels and/or (n,α) reactions that lead to neutron unbound states in ^{9}Be. The dominantly isolated peak at the high energy in top four panels of the spectra is from the ^{12}C(n,α)^{9}Be reaction, while the highest energy peak in the $E_n \approx 8.45$ MeV data is due to ^{13}C(n,α)^{10}Be.

C. (n,p),(n,α),(n,d) reactions

Various works [24, 25, 35, 36] highlight the application of diamond detectors, as an active carbon target, to not only validate past experimental data on ^{12}C(n,α) but to provide new experimental data on ^{12}C(n,p), ^{12}C(n,d) [25, 35, 36] , and ^{13}C(n,α) [24, 25] using quasi-mono-energetic neutron beams.

To better identify the contributions from particular reaction channels, it is useful to project the reconstructed reaction Q-value rather than detected energy. In this case we simply plot the difference in detected energy from the reconstructed neutron energy, as shown in the projection of incident neutron energies between 18 and 20 MeV in Fig. 8.

The ^{12}C(n,α) threshold is at $E_n > 6.2$ MeV and the peak from this reaction channel is cleanly separated from other reaction channels at E_n above 8.2 MeV. Below 8.2 MeV, events due to elastic and inelastic scattering form a background underneath the (n,α) peak, as shown in Fig. 9. Here, we make an assumption that the shape of the elastic and inelastic scattering contributions to the pulse height spectrum is consistent with the simulation and we can then fit the experimental data to determine the (n,α_0) contribution, as shown in Fig. 9. The resulting experimental yields and normalized cross sections are

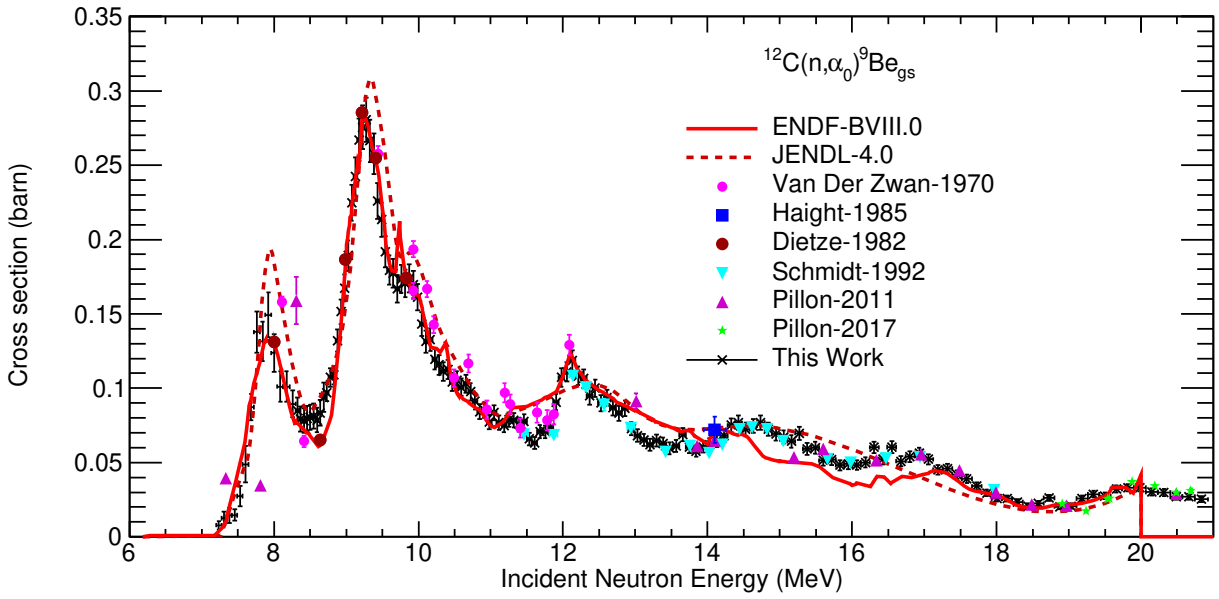

FIG. 10. The ^{12}C(n,α_0) yields are normalized relative to the energy-dependendent incident neutron flux as given by ionization chamber flux monitors. The overall normalization is chosen so that the cross section matches the weighted average of experimental data at 14.1 MeV [25, 37–40] , 63.6 ± 3.1 mb. After this normalization, the diamond data is in excellent agreement with various experimental data [25, 35, 37, 38, 42, 43] over the entire range from threshold to 20 MeV and in good agreement with ENDF/B-VIII.0. Consistent with past measurements, ENDF/B-VIII.0 appears to slightly underestimate the cross section between 14.5 and 18 MeV and slightly overestimate the cross section between 11 and 14 MeV.

presented in the following section, with an additional 10% uncertainty adopted to the data points below 8.2 MeV to account for this method of subtracting the other reaction channels.

V. RESULTS

A. Normalization

The relative flux normalization over the entire energy range is obtained from measurements of the ^{238}U(n,f) and ^{235}U(n,f) fission reactions with an ionization chamber. The ionization chambers were located approximately 2 m further downstream of the diamond detector. Expected differences, due to downscatter and finite target size, in the energy shape of the neutron flux at the different positions was characterized with an MCNP simulation of the flight path and is estimated to be less than 3%. Due to uncertainties with respect to overlap between the diamond detector and the neutron beam-spot, the detector thickness, and the detector active area, we obtain the overall normalization, $N_b \times \rho_{12C} \times \epsilon_0$ by normalizing the measured yield for the ^{12}C(n,α) reaction at 14.1 MeV to the weighted average of experimental data from Refs. [25, 37–40] as provided in the EXFOR [41] database. Here the ϵ_0 term describes the efficiency for detecting the full energy of ^{9}Be and α recoils. Corrections to the efficiency term are determined independently for each reaction channel, as a function of incident neutron energy, as described in Section V C. Thus, there is a relative normalization uncertainty of approximately 5% that comes from the relative shape of the neutron flux (3%) and the relative detection efficiency (4%).

TABLE II. Summary of past experimental data on ^{12}C(n,α_0) around 14.1 MeV, as given by the EXFOR database [41], that was used to normalize the experimental data in this work.

Reference	E_n	σ
Schmidt *et al.* [37]	14.02 ± 0.03	56.5 ± 1.9
Schmidt *et al.* [37]	14.2 ± 0.04	62 ± 2.1
Haight *et al.* [38]	14.10 ± 0.15	72 ± 9
Sanami *et al.* [39]	14.10	70 ± 7
Pillon *et al.* [25]	14.10 ± 0.01	64.7 ± 3.2
Kondo *et al.* [40]	14.2 ± 0.2	69 ± 6
Weighted Average	14.1	63.6 ± 3.1

The experimental data from Ref. [37], which is derived from time-reversed (α,n$_0$) data and has the lowest uncertainties, is averaged between the values at 14.0 and 14.2 MeV before taking the weighted average with other measurements at 14.1 MeV. The weighted-average that we obtain is 63.6 ± 3.1 mb and from this we obtain our

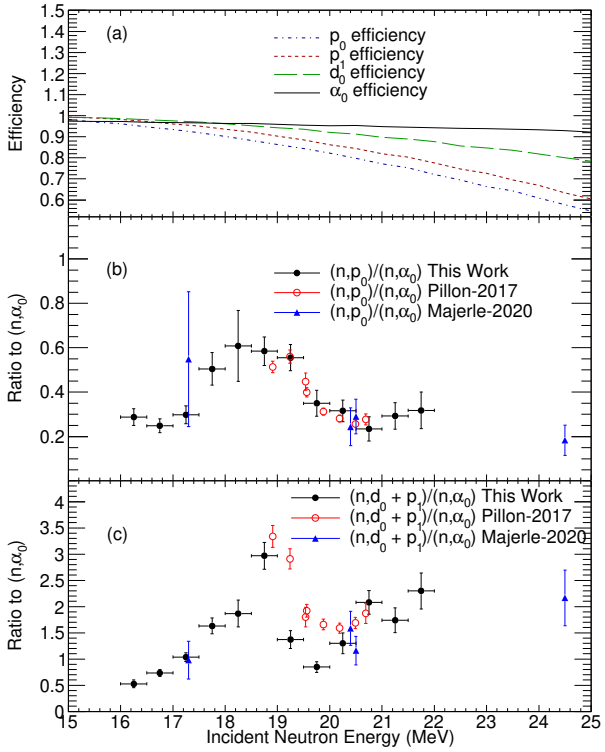

FIG. 11. The ratio of ^{12}C(n,p$_0$) to ^{12}C(n,α_0) from this work is shown in the panel (b) and is in excellent agreement with the results of Ref. [35] and [36], also taken with a diamond detector. In the panel (c), the ratio of the summed d_0 + p_1 reaction channels relative to α_0 is shown in comparison with the results of Ref. [35] and [36]. The overall trend is consistent with their work although the scale is slightly inconsistent. Finally, the relative efficiency for detecting the full energy of the different reaction channels is shown in panel (a).

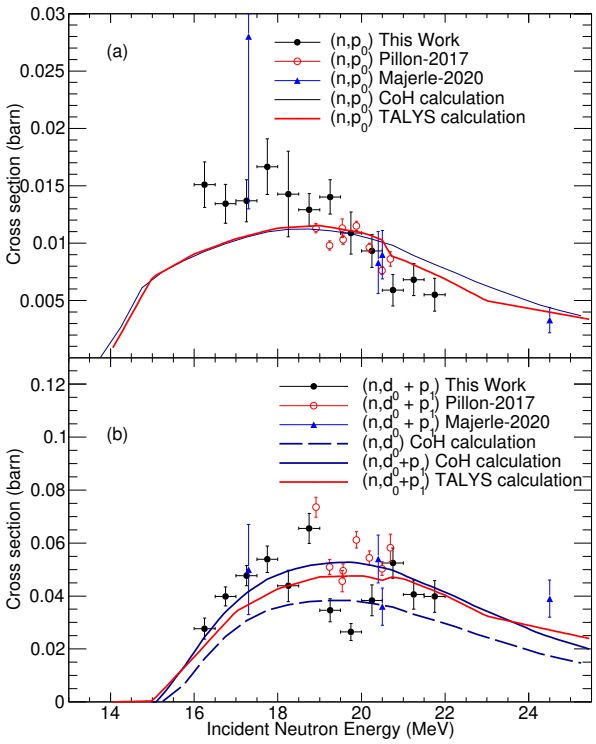

FIG. 12. Partial cross sections, derived from the ratios from Fig. 11, for the (n,p_0) and (n,d_0 + p_1) reaction channels are shown in the top and bottom panels, respectively. In addition, the results are compared with statistical Hauser-Feshbach calculations using the CoH [45] and TALYS [46] with all default parameters.

value for the product of $N_b \times \rho_{12C} \times \epsilon_0$ such that the measured yields correspond to this value for the cross section.

B. ^{12}C(n,α_0)^{9}Be$_{gs}$

With the overall normalization from the previous section, the experimental data is in good agreement with the two works of Pillon *et al.* between 12 and 20 MeV and in general with the ENDF/B-VIII.0 evaluation, as shown in Fig. 10. Consistently shown with the work of Refs. [25] and [37], the evaluation appears to slightly underestimate the cross section between 14.5 and 18 MeV and slightly overestimate the cross section between 11 and 14 MeV. However, the data shows excellent agreement with ENDF/B-VIII.0 and experimental data from Ref. [42] between 8 MeV and 11 MeV. In Fig. 10, and the corresponding Table III, the uncertainty on the cross section reflects the relative normalization uncertainty and statistical uncertainty, but not the uncertainty from the overall normalization.

C. ^{12}C(n,p$_0$) and ^{12}C(n,d$_0$+p$_1$)

At neutron energies above 15 MeV, ^{12}C(n,p$_0$) and ^{12}C(n,a$_0$) are well isolated from other charged particle reaction channels whereas the ^{12}C(n,d$_0$) could not be discriminated from the ^{12}C(n,p$_1$) reaction. The ratios of the yields from the different reaction channels are shown in Figs. 11b and 11c, relative to the ^{12}C(n,α_0) channel, with efficiency corrections as shown in Fig. 11a. Here, the efficiency for each channel was determined in a manner similar to that described in Majerle *et al.* [36], assuming an isotropic distribution (in the c.m. frame), and tallying the reaction products that deposit their full energy within the volume of the diamond detector. In their work, they also discuss the extreme case in which the detection efficiency for each reaction channel is reduced if the outgoing charged particles were emitted entirely at zero degrees (corresponding to the maximum outgoing energy for the light charged particle). However, the uncertainty in the efficiency correction, due to the absence of angular distribution information at each energy,

is estimated to be around 4% up to 22 MeV based on the general shape of past differential cross section data [38, 44] for (n,α), in contrast to this extreme case. From this efficiency correction, and the normalization from the previous section, the partial cross sections for (n,p_0) and the sum of (n,d_0+p_1) are obtained and shown in Fig. 12 and given in Table IV. The results are in good agreement with the most recent work of Pillon *et al.* [35] and Ref. [36]. In addition, the data is in reasonably good agreement with statistical Hauser-Feshbach calculations that were performed using the CoH [45] and TALYS [46] codes with all default parameters. For the (n,d_0+p_1) cross section, the effective efficiency was estimated assuming that the ratio between p_0:p_1 is consistent with the statistical model calculations, thus constraining the expected (n,p_1) contribution to the summed (p_1 + d_0) yield.

D. ^{13}C(n,α_0)^{10}Be$_{gs}$

Finally, the ^{13}C(n,α_0) reaction could be measured up to approximately 11 MeV and the measured cross sections, once again normalized to ^{12}C(n,α_0) as described in Section V A, are shown in Fig. 13 and Table V. An isotopic abundance of 1.07% is adopted for determining the number of ^{13}C atoms relative to ^{12}C. Here, the scale of the evaluated ^{13}C(n,α_0) partial cross section from ENDF/B-VIII.0 is in relatively good agreement with the data up to about 9 MeV, but significantly overestimates the data at higher energies. The trend established by the current experimental data above 10 MeV appears to be in good agreement with the previous data taken at 14 and 17 MeV [24, 25]. The previous data [24] taken with a diamond detector at these energies made use of pulse shape analysis to reduce the backgrounds that in the current analysis prohibit us from extracting a cross section at these energies. By looking back at the comparison with simulations in Fig. 4, had the partial cross section been as large as predicted by the evaluation, the signal to background ratio likely would have been good enough to measure some yield. In addition, the results that we present are in good agreement with the general upper limits that are presented in the work of Resler *et al.* [47] where the limits are based on what is leftover from the total neutron cross-sections after subtracting contributions from elastic scattering and (n,2n). At these lower energies, the cross sections reported by Pillon *et. al* are much larger than our data and the upper limits established by Resler. Along with the data taken at the 90L flight path at a distance of 7.618 m, results from a separate experiment with the diamond detector located on the 15R flight path of WNR at a distance of 14.371 m is also shown in Fig 13. Data was recorded for a longer period of time so the statistical uncertainties are improved. The results from this additional study are consistent with the 90L results for ^{12}C(n,α_0), however, the data was recorded with higher thresholds that would've precluded a complete discussion on the elastic and inelastic channels as discussed in Section IV. As a result, we have limited this current work to primarily focus on the 90L dataset.

In order to improve theoretical representations of the current data, the resonance analysis was performed using a R matrix code, AZURE [48] with Brune parameterizations [49]. Energy relevant inelastic scattering data sets [47, 50] were included during the simultaneous fit to constrain R-matrix parameters at this high excitation energy in ^{14}C ($E_x = 14-20$ MeV). In Fig. 14, the (n,α_0) channel is shown in the panel (a), and the inelastic scattering channels of the excited states in ^{13}C, E_x = 3.09, 3.68, and 3.85 MeV, are shown in panels (b), (c), and (d), respectively. Because the current data was obtained as angle integrated measurements and the level information at this high excitation energy is quite limited, the R-matrix analysis was fitted to total (n,α_0) and (n,n$'$) cross sections. Overall fit confidence resulted in a reduced chi-squared per degree of freedom of less than 1 for each of the individual channels. R-matrix fit results confirmed the resonance structures shown in the (n,α_0) channel are prominently populated in (n,n$'$) channels as well. A full R-matrix analysis combining with low energy elastic scattering data in differential cross sections would provide a consistent R-matrix parameter set, however this is beyond the scope of the current work. A recent effort to characterize the ^{14}C system with an R-matrix analysis is presented in the work of Ref. [51], which is based on the neutron scattering data [47, 50] and the inverse (α,n_0) cross section data from the thesis work of Guillemette [52]. The present ^{13}C(n,α_0) data is found to be in good agreement with the scale and trend of the angle-integrated (α,n_0) cross section data from that work and will provide a complementary data set when correlating the (α,n_0) differential data with the total neutron cross section data.

VI. CONCLUSIONS AND OUTLOOK

We report new relative cross sections for the ^{12}C(n,α_0) reaction that ties together past experimental data, all the way from threshold up to 20 MeV, with high resolution. For the purposes of using a diamond detector as a neutron spectrometer, monitoring neutrons via (n,α_0), this information is crucial for establishing this reaction as a standard at these energies. In addition, the elastic scattering data on carbon is considered a standard only up to approximately 1.8 MeV. It is clear that the use of elementally pure diamond detectors that are simultaneously sensitive to multiple reaction channels will continue to serve as an excellent tool for validating evaluations of the ^{12,13}C + n system. Specifically, by applying a forward propagation method to compare the experimental data with simulations, which take data evaluations as inputs, can be used to infer the necessary modifications to the corresponding evaluations. Relative cross sections for ^{12}C(n,p_0), ^{12}C(n,d_0 + p_1) and ^{13}C(n,α_0) reaction chan-

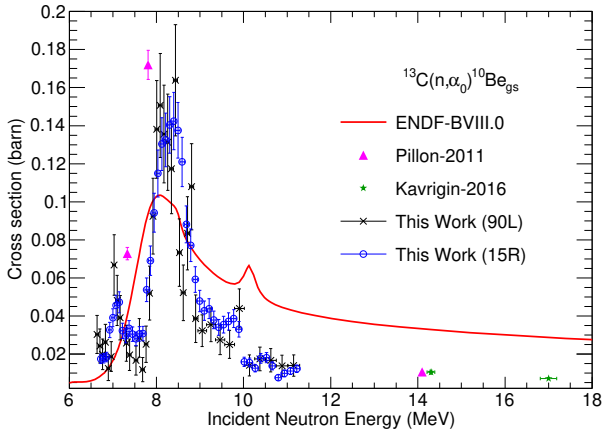

FIG. 13. The results for the ^{13}C(n,α_0) partial cross section from this work (blue and black) are shown in comparison to experimental results from Refs. [25] and [24]. The trend of the experimental data from this work towards the data points at high energy show a consistent trend. The partial cross section from ENDF shows good agreement with the overall scale of the data below 10 MeV, however, it significantly overestimates the cross section at higher energies.

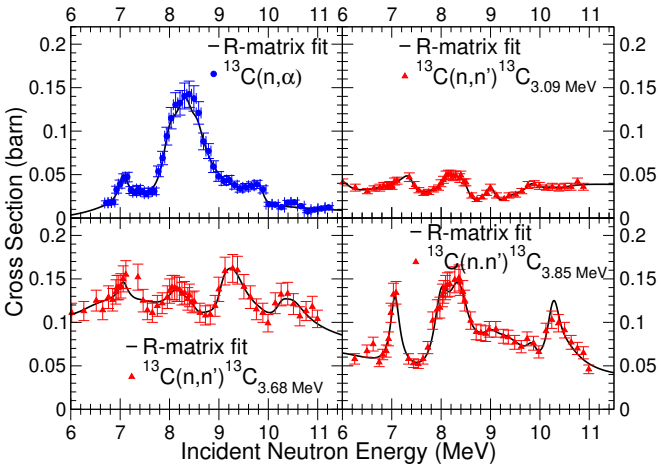

FIG. 14. The results for the ^{13}C(n,α_0) partial cross section from this work are shown in comparison to R-matrix fits together with ^{13}C(n,n$'$) reactions at the relevant neutron energy range. The inelastic scattering data is from Resler *et al.* [47]. The vertical axis is shown in the fixed scale for all panels.

nels are also reported that are in good agreement with previous diamond detector data while also extending the measurements to new energies. Due to the growing interest in the use of diamond detectors as neutron spectrometers, it is clear that ENDF/B-VIII.0 should be modified at energies beyond the previous R-matrix analysis, above 6 MeV, to better reproduce the new experimental data. However, any modifications should also be bench-marked against other applications such as detector response functions from organic scintillators.

ACKNOWLEDGMENTS

This work benefits from the LANSCE accelerator facility and is supported by the U.S. Department of Energy under contract No. 89233218CNA000001, by the Laboratory Directed Research and Development program of Los Alamos National Laboratory under project number 20180228ER, and by the US Nuclear Data Program under the Office of Science of U.S. Department of Energy. The authors would like to thank Dr. R. J. deBoer from the University of Notre Dame for the AZURE help and Dr. T. N. Massey from the Ohio University for sharing past ^{13}C(n,α) data.

[1] P. W. Lisowski, C. D. Bowman, G. J. Russell, and S. A. Wender. Nuclear Science and Engineering, 106(2):208–218 (1990)
[2] H. I. Kim *et al.* Nuclear Instruments and Methods in Physics Research Section A, Volume 963, 163699 (2020)
[3] A. Georgiadou *et al.*, Bull. Am Phys. Soc. 64, 12 (2019)
[4] H. Y. Lee, S. Mosby, R. C. Haight, and M. C. White, EPJ Web of Conferences, Volume 122, 05004 (2016)
[5] S. A. Kuvin *et al.* Phys. Rev. C. 102, 024623 (2020).
[6] S. A. Kuvin *et al.*, Bull. Am Phys. Soc. 64, 12 (2019)
[7] H. Y. Lee, S. Mosby, T. Kawano, R. C. Haight, and B. Manning, JPS Conf. Proc. 14, 020512 (2017)
[8] W. Adam et al., Nucl. Instrum. Methods A514, 79 (2003).

[9] M. Angelone, M. Pillon, M. Marinelli, E. Milani, A. Paoletti, A. Tucciarone, G. Pucella, G. Verona-Rinati, Radiation Protection Dosimetry, Volume 110, Issue 1-4, 1 August 2004, Pages 233–236.

[10] Bednarczyk *et al*, Acta Physica Polonica B, vol. 38, Issue 4, p.1293, April 2007

[11] M. Rebisz-Pomorska, M. Ciobanu, M. Kis, M. Pomorski, B. Voss, Nuclear Instruments and Methods in Physics Research Section A, Volume 620, Issues 2–3, 2010, Pages 534-539, ISSN 0168-9002.

[12] C. Cazzaniga *et al.* Review of Scientific Instruments 85(11):11E101 (2014)

[13] M.Osipenko et.al, Nuclear Instruments and Methods in Physics Research Section A, 799, 207 (2015), arXiv:1505.06654

[14] Berlev, A.I., Rodionov, N.B., Tyutyunnikov, S.I. et al. Phys. Part. Nuclei Lett. 13, 352–357 (2016).

[15] Pillon et al. Fusion Engineering and Design, Volume 106, 2016, Pages 93-98, ISSN 0920-3796.

[16] R. V. Wagoner, Astrophysical Journal Supplement Series. No. 162, Volume 18, 247 (1969)

[17] www.cividec.at

[18] H. Y. Lee *et al.*, submitted to Nuclear Instruments and Methods in Physics Research Section A.

[19] C. Weiss *et al.* Nuclear Data Sheets, Volume 120, Pages 208-210 (2014).

[20] C. Weiss. CERN Thesis, (2014)

[21] Rebai *et al.* 2015 JINST 10 C03016

[22] S.A. Wender *et al.* Nuclear Instruments and Methods in Physics Research Section A, 336(1):226 – 231 (1993).

[23] H. Jansen, Ph.D. thesis, Rheinische Friedrich-Wilhelms-Universität Bonn (2013).

[24] P. Kavrigin *et al.*, Eur. Phys. J. A. 52:179 (2016) doi.org/10.1140/epja/i2016-16179-9

[25] M. Pillon *et al.* Nucl. Instrum. Methods Phys. Res. A, 640 (1) (2011), pp. 185-191

[26] S. Agostinelli *et al.* GEANT4: A Simulation toolkit. Nuclear Instruments and Methods in Physics Research Section A, 506:250–303, (2003)

[27] D. A. Brown *et al.* *Nuclear Data Sheets*, 148:1 – 142, 2018. Special Issue on Nuclear Reaction Data.

[28] A. R. Garcia *et al.*, Nuclear Inst. and Methods in Physics Research, A 868 (2017) 73–81.

[29] G. Dietze, H. Klein, NRESP4 and NEFF4: Monte Carlo codes for the calculation of neutron response functions and detection efficiencies for NE213 scintillation detectors, Physikalisch-Technische Bundesanstalt (PTB), PTB-ND-22, Braunschweig, Germany, 1982.

[30] M. Zboril *et al.*, Proceedings of Science (240) - 1st EPS conference on Plasma Diagnostics (ECPD2015)

[31] GEANT4 Physics Reference Manual

[32] K. Shibata *et al.*. *Journal of Nuclear Science and Technology*, 48(1):1–30, 2011.

[33] E. Pirovano *et al.*. Physical Review, Part C, Nuclear Physics, 99, 024601 (2019)

[34] F. G. Perey, W. E. Kinney. U.S.AEC Nucl.Cross Sections Advisory Comm. Repts, No.42, p.190 (1978) EXFOR:23365.002

[35] M. Pillon *et al.* EPJ Web of Conferences 146, 11005 (2017)

[36] Majerle *et al.* Nuclear Inst. and Methods in Physics Research, A 951 (2020) 163014

[37] D. Schmidt, R. Boettger, H.Klein, and R.Nolte, Rept: Phys.Techn.Bundesanst., Neutronenphysik Reports, No.8 (1992). (exfor 23228.002)

[38] R. C. Haight, S. M. Grimes, R. G. Johnson, and H. H. Baschal, Nuclear Science and Engineering, 87:1, 41-47 (1984).

[39] T. Sanami, B. Mamoru,K. Saito, and N. Hirakawa, Nucl. Instrum. Methods Phys. Res. A, Volume 440, Issue 2, 1 February 2000, Pages 403-408

[40] K. Kondo *et al.* Journal of Nuclear Science and Technology, 45:2, 103-115 (2008)

[41] N. Otuka *et al.* Nucl. Data Sheets 120(2014)272 .

[42] G. Dietze, H. J. Brede, H. Klein, H. Schoelermann. Conf.on Nucl.Data for Sci.and Technol.,Antwerp 1982, p.930 (1982). (EXFOR 21823.002)

[43] L. Van der Zwan and K.W. Geiger. Nuclear Physics A 152(3) (1970).

[44] Salathe *et al.* Jour. Helvetica Physica Acta, Vol.43, p.437 (1970).((EXFOR 20517.002)

[45] T. Kawano, CoH_3: The Coupled-Channels and Hauser-Feshbach Code.

[46] A.J. Koning *et al.* AIP Conference Proceedings 769, 1154 (2005)

[47] D. A. Resler, H. D. Knox, P. E. Koehler, R. O. Lane, and G. F. Auchampaugh, Phys. Rev. C 39 (1989) 766.

[48] R. E. Azuma, E. Uberseder, E. C. Simpson, C. R. Brune, H. Costantini, R. J. de Boer, J. Görres, M. Heil, P. J. LeBlanc, C. Ugalde, M. Wiescher, Phys. Rev. C 81 (2010) 045805

[49] C. R. Brune, Phys. Rev. C 66, 044611 (2002)

[50] R. O. Lane, H. D. Knox, P. Hoffmann-Pinther, R. M. White, and G. F. Auchampaugh, Phys. Rev. C 23 (1981)1883.

[51] T. N. Massey, J. F. Guillemette, S. M. Grimes, and J. E. O'Donnell, AIP Conference Proceedings 769 (2005) 450

[52] James F. Guillemette, *A study of the Higher Excitation Level in ^{14}C via the $^{10}Be(\alpha,n)^{13}C$ Reaction*, Ph.D. thesis, Ohio University (1994).

TABLE III: Reaction cross sections for ^{12}C(n,α_0)^{9}Be normalized to past ^{12}C(n,α_0)^{9}Be experimental data around 14 MeV.

E_n	σ (mb)
7.24	7.8 ± 2.8
7.31	12.5 ± 4.4
7.38	14.4 ± 5.1
7.46	14.6 ± 3.7

Table III. Cont.

7.53	27.4 ± 6.9
7.61	48.8 ± 12.3
7.68	87.3 ± 8.9
7.76	137.8 ± 14.0
7.84	131.5 ± 13.3
7.92	149.3 ± 15.1
8.01	123.7 ± 12.6
8.09	101.1 ± 10.3
8.17	101.1 ± 10.3
8.26	89.5 ± 9.1
8.32	84.9 ± 8.9
8.37	79.2 ± 8.3
8.41	78.2 ± 8.2
8.46	79.7 ± 8.4
8.50	80.5 ± 8.4
8.55	81.2 ± 8.5
8.59	78.5 ± 8.2
8.64	83.4 ± 8.7
8.69	93.8 ± 9.8
8.73	96.9 ± 5.6
8.78	107.3 ± 6.1
8.83	109.0 ± 6.2
8.88	132.0 ± 7.4
8.93	151.4 ± 8.3
8.98	167.4 ± 9.1
9.02	189.3 ± 10.2
9.07	224.8 ± 12.0
9.12	242.3 ± 12.9
9.18	267.1 ± 14.1
9.23	275.6 ± 14.6
9.28	280.7 ± 14.8
9.33	266.4 ± 14.1
9.38	257.7 ± 13.7
9.43	226.1 ± 12.1
9.49	213.4 ± 11.5
9.54	191.9 ± 10.4
9.60	179.5 ± 9.8
9.65	177.4 ± 9.7
9.71	166.9 ± 9.2
9.76	173.5 ± 9.5
9.82	170.4 ± 9.3
9.87	173.9 ± 9.5
9.93	169.7 ± 9.3
9.99	161.4 ± 8.9
10.05	143.1 ± 8.0
10.10	131.4 ± 7.4
10.16	132.7 ± 7.5
10.22	119.4 ± 6.8
10.28	115.7 ± 6.6
10.34	111.2 ± 6.4
10.40	112.7 ± 6.5
10.47	104.1 ± 6.0
10.53	105.2 ± 6.1
10.59	100.7 ± 5.9
10.66	103.0 ± 6.0
10.72	97.6 ± 5.7
10.78	91.1 ± 5.4
10.85	84.2 ± 5.1
10.91	85.2 ± 5.1
10.98	77.2 ± 4.7
11.05	83.5 ± 5.0
11.12	76.9 ± 4.7

Table III. Cont.

11.18	74.8 ± 4.6
11.25	78.8 ± 4.8
11.32	78.6 ± 4.8
11.39	75.5 ± 4.6
11.46	77.7 ± 4.8
11.53	65.9 ± 4.1
11.61	63.3 ± 4.0
11.68	70.9 ± 4.4
11.75	70.6 ± 4.4
11.83	73.8 ± 4.6
11.90	90.5 ± 5.4
11.98	107.3 ± 6.3
12.05	111.1 ± 6.5
12.13	118.6 ± 6.9
12.21	108.4 ± 6.3
12.29	106.5 ± 6.2
12.37	94.7 ± 5.7
12.45	100.0 ± 5.9
12.53	90.1 ± 5.4
12.61	93.6 ± 5.6
12.69	86.8 ± 5.3
12.78	83.2 ± 5.1
12.86	86.4 ± 5.2
12.94	72.9 ± 4.6
13.03	68.2 ± 4.3
13.12	65.1 ± 4.2
13.20	61.9 ± 4.0
13.29	64.7 ± 4.1
13.38	62.6 ± 4.0
13.47	59.5 ± 3.9
13.56	61.2 ± 4.0
13.66	68.7 ± 4.4
13.75	60.3 ± 3.9
13.84	57.6 ± 3.8
13.94	60.5 ± 3.9
14.03	62.1 ± 4.3
14.13	64.3 ± 4.0
14.23	68.0 ± 4.3
14.33	75.1 ± 4.7
14.43	76.7 ± 4.8
14.53	72.4 ± 4.6
14.63	74.5 ± 4.7
14.74	77.0 ± 4.8
14.84	72.4 ± 4.6
14.95	69.1 ± 4.4
15.05	67.2 ± 4.3
15.16	64.2 ± 4.1
15.27	69.7 ± 4.4
15.38	59.2 ± 3.9
15.49	59.9 ± 3.9
15.60	51.4 ± 3.5
15.72	52.0 ± 3.5
15.83	48.2 ± 3.3
15.95	48.9 ± 3.4
16.07	48.3 ± 3.3
16.19	50.1 ± 3.4
16.31	60.2 ± 3.9
16.43	52.4 ± 3.5
16.55	60.3 ± 3.9
16.68	50.8 ± 3.5
16.80	54.1 ± 3.6
16.93	56.3 ± 3.7

Table III. Cont.

17.06	52.2 ± 3.5
17.19	45.1 ± 3.2
17.32	45.8 ± 3.2
17.45	41.9 ± 3.0
17.59	39.1 ± 2.8
17.73	34.1 ± 2.6
17.86	29.5 ± 2.3
18.00	25.9 ± 2.1
18.15	25.7 ± 2.1
18.29	23.5 ± 2.0
18.43	20.7 ± 1.8
18.58	22.4 ± 1.9
18.73	26.2 ± 2.1
18.88	20.3 ± 1.8
19.03	20.7 ± 1.8
19.19	25.9 ± 2.1
19.34	28.7 ± 2.3
19.50	27.5 ± 2.2
19.66	32.2 ± 2.5
19.82	33.0 ± 2.5
19.98	33.2 ± 2.5
20.15	30.2 ± 2.3
20.32	29.7 ± 2.3
20.49	27.0 ± 2.2
20.66	27.0 ± 2.2
20.83	25.2 ± 2.1
21.01	22.7 ± 1.9
21.19	25.2 ± 2.1
21.37	24.1 ± 2.0
21.56	20.9 ± 1.8

TABLE IV. Partial cross sections for ^{12}C(n,p$_0$) and ^{12}C(n,p$_1$+d$_0$), measured relative to the ^{12}C(n,α_0)^{9}Be reaction channel.

E_n	(n,d$_0$+p$_1$) σ (mb)	(n,p$_0$) σ (mb)
16.25	27.7 ± 4.0	15.1 ± 2.0
16.75	39.8 ± 3.6	13.4 ± 1.7
17.25	47.7 ± 3.8	13.7 ± 1.8
17.75	53.9 ± 5.0	16.7 ± 2.4
18.25	43.8 ± 6.0	14.3 ± 3.7
18.75	65.5 ± 5.6	12.9 ± 1.4
19.25	34.6 ± 4.3	14.0 ± 1.5
19.75	26.4 ± 3.2	10.9 ± 1.8
20.25	38.3 ± 5.8	9.3 ± 1.4
20.75	52.4 ± 5.7	5.9 ± 1.4
21.25	40.6 ± 5.5	6.8 ± 1.4
21.75	39.8 ± 6.0	5.5 ± 1.4

TABLE V. Reaction cross sections for ^{13}C(n,α_0)^{10}Be measured relative to the ^{12}C(n,α_0)^{9}Be reaction channel, normalized to past experimental data around 14.1 MeV.

E_n	σ (mb)
6.72	17.4 ± 2.4
6.79	17.8 ± 2.5
6.86	18.3 ± 2.5
6.93	32.6 ± 4.0
7.00	39.0 ± 4.7
7.07	45.5 ± 5.3
7.14	47.2 ± 5.5
7.22	32.2 ± 4.0
7.29	29.5 ± 3.7
7.37	33.4 ± 4.1
7.45	30.4 ± 3.8
7.53	28.0 ± 3.6
7.61	30.5 ± 3.8
7.69	30.7 ± 3.8
7.78	53.7 ± 6.2
7.86	69.1 ± 7.7
7.95	94.2 ± 10.3
8.03	114.9 ± 12.3
8.12	130.3 ± 13.9
8.21	132.5 ± 14.1
8.30	140.4 ± 14.9
8.40	142.4 ± 15.1
8.49	137.6 ± 14.6
8.59	120.9 ± 12.9
8.69	88.1 ± 9.7
8.79	77.1 ± 8.6
8.89	59.1 ± 6.8
8.99	47.8 ± 5.6
9.10	42.7 ± 5.1
9.21	43.8 ± 5.2
9.32	37.9 ± 4.6
9.43	34.0 ± 4.2
9.54	35.4 ± 4.4
9.66	37.1 ± 4.5
9.77	38.6 ± 4.7
9.89	33.0 ± 4.1
10.01	15.9 ± 2.4
10.14	15.5 ± 2.3
10.27	12.5 ± 2.0
10.39	17.7 ± 2.6
10.53	18.1 ± 2.6
10.66	13.7 ± 2.1
10.80	7.6 ± 1.4
10.93	9.8 ± 1.7
11.08	11.0 ± 1.9
11.22	12.3 ± 2.0